The 8th European Congress on Computational Methods in Applied Sciences and Engineering
ECCOMAS Congress 2022
5–9 June 2022, Oslo, Norway

ENERGY-MOMENTUM CONSERVING DYNAMIC VARIATIONAL MODELING OF FIBER-BENDING STIFFNESS IN COMPOSITES

INIYAN KALAIMANI[1], JULIAN DIETZSCH[1] AND MICHAEL GROSS[1]

[1] Technische Universität Chemnitz
Professorship of applied mechanics and dynamics
Reichenhainer Strasse 70, 09126 Chemnitz, Germany
e-mail: iniyan.kalaimani@mb.tu-chemnitz.de,
julian.dietzsch@mb.tu-chemnitz.de,
michael.gross@mb.tu-chemnitz.de

Key words: Fiber reinforced composites, Fiber-bending stiffness, energy-momentum time integration, higher-order finite elements in space and time, Mixed variational principle

Abstract. We propose a new variational formulation for large deformations in dynamical systems made of 3D-fiber-reinforced composites. The formulation emanates from the dynamic variational approach based on the principle of virtual power. The use of higher-order gradient theory along with multi-field mixed-finite element method enables us to model the fiber-bending stiffness in fiber reinforced composites for numerical simulations accurately. Our proposed model capture higher-order energy contributions exhibited by fibers that influence the fiber-bending curvature, and consequently the fiber-bending stiffness behaviour. For this, we introduce a higher-order gradient of the deformation mapping as an independent field in the internal energy functional formulation. Along with the energy-momentum scheme, our new time integrator makes possible to perform long-term dynamic simulations with larger time steps and efficient CPU-time. We demonstrate our model using transient dynamical simulations on thre geometrical examples that exhibit hyperelastic, transversely isotropic, polyconvex gradient material behaviour. In the first example, a cantilever beam is self-excited due to its body weight, in the second, a L-shaped block tumbles free in the ambient space after an initial loading phase and in the third a turbine rotor is rotated due to hydrodynamic pressure. It is observed that our model conserves total momenta and total energy and preserves their time evolution in all these examples along with spatial and temporal convergence.

1 INTRODUCTION

Fibre-reinforced composites are in high demand in many industrial applications because of the reinforcement properties of fibres which enhance, to mention a few, the stiffness and strength-to-weight ratio of a structure. On the simulation point of view, this creates a demand to find efficient numerical solving methods to predict the behaviour of these kind of materials. Avoiding locking behavior in finite elements was one of the challenging aspect in recent times that is now addressed by many modern finite element codes. However, the usage of the same is less understood in the dynamic regime which could significantly improve the accuracy and efficiency

in dynamical simulations. In order to achieve this while computing the influence of various geometrical and material non-linearities, necessary modificaition of the standard continuum is inevitable. At the same time, any modification of the standard continuum has to satisfy corresponding physical balance laws. Recent developments in the energy-momentum scheme provide a better opportunity to address these problems in a dynamic regime. With this motivation,

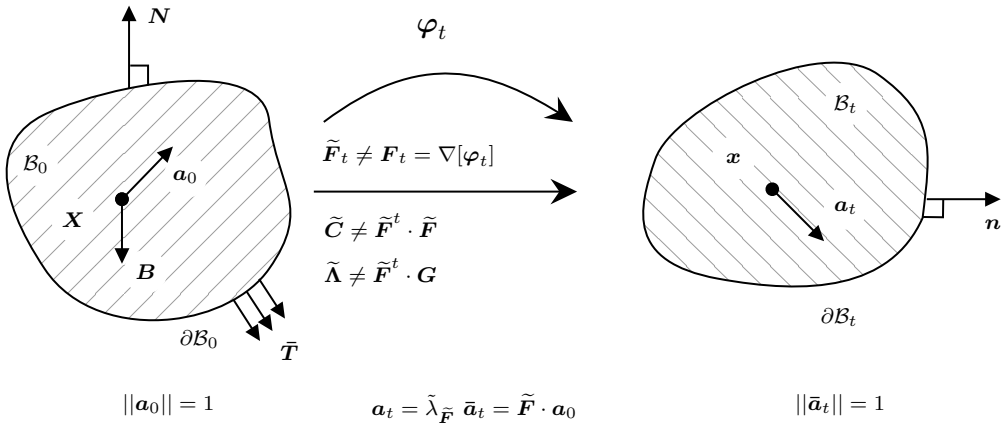

Figure 1: Transversely isotropic continuum with fibers oriented in direction of $\boldsymbol{a}_0$ and element-wise independent deformation gradient.

our current work is focused on improving numerical methods to enhance the application of the lightweight design of rotating systems made of fiber-reinforced composites. The experimental outcome of the three-point bending test point out that the fiber induced deformation patterns on mesoscopic level influence the macroscopic bending stiffness in fiber-reinforced composites [2]. Based on this outcome, we set our problem statment to capture the fiber bending stiffness in dynamical problems, which would help us reduce the unaccounted out-of-plane bending rigidity of an arbitrary geometry. Analogous to the work of [3], where static problem has been addressed, we begin with assuming a constitutive model to capture the fiber bending stiffness. Here the strain energy function takes not only the strain and fiber direction into account, but also the information of fiber-curvature(see Figure 1). A transversely isotropic continuum $\boldsymbol{\mathcal{B}}_0$ is considered with fibers at each point of the continuum oriented in direction of vector $\boldsymbol{a}_0$ in material configuration. In contrast to [3], we introduced a deformation gradient $\widetilde{\boldsymbol{F}}$ as an element-wise independent field in our Hu-Washizu based internal energy functional in [6]. Similarly, $\widetilde{\boldsymbol{\Gamma}}$ is introduced as an independent mixed field for $\nabla_{\boldsymbol{X}}[\widetilde{\boldsymbol{F}}]$ to capture fiber curvature effects. In this work, we propose an additive split of strain energy function in terms of $\widetilde{\boldsymbol{C}}$ and $\widetilde{\boldsymbol{\Lambda}}$ as,

$$\Psi^{\text{total}}(I_i(\widetilde{\boldsymbol{C}}, \widetilde{\boldsymbol{\Lambda}})) \;=\; \Psi^{\text{iso}}(I_1(\widetilde{\boldsymbol{C}}), I_2(\widetilde{\boldsymbol{C}}), I_3(\widetilde{\boldsymbol{C}})) + \;\Psi^{\text{hg}}(I_6(\widetilde{\boldsymbol{\Lambda}})), \tag{1}$$

which is in line with the variation of [3], where $I_6 := \boldsymbol{k}_0 \cdot \boldsymbol{k}_0$, $\boldsymbol{k}_0 := (\widetilde{\boldsymbol{\Lambda}} \cdot \boldsymbol{a}_0)$ and $\widetilde{\boldsymbol{\Lambda}}$ is an independent mixed field for $\boldsymbol{\Lambda} := \widetilde{\boldsymbol{F}}^t \cdot \boldsymbol{G}$ which is the pure referential representation of $\boldsymbol{G}$. $\boldsymbol{G}$ is defined as the referential gradient of the spatial fiber direction vector $\nabla_{\boldsymbol{X}} \boldsymbol{a}_t$ with $\boldsymbol{a}_t = \tilde{\lambda}_{\widetilde{\boldsymbol{F}}}\ \bar{\boldsymbol{a}}_t$

and $\tilde{\lambda}_{\widetilde{\boldsymbol{F}}}$ is the fiber stretch. Thus, $\boldsymbol{\Lambda} = \widetilde{\boldsymbol{F}}^t \cdot \Big[\boldsymbol{a}_0 \cdot \nabla_{\boldsymbol{X}}[\widetilde{\boldsymbol{F}}^t] + \widetilde{\boldsymbol{F}} \cdot \nabla_{\boldsymbol{X}} \boldsymbol{a}_0\Big]$.

I_1, I_2, I_3 are the usual isotropic principal invariants based on the right Cauchy green tensor $\widetilde{\boldsymbol{C}}$, which is a mixed field variable for $\boldsymbol{C} = [\widetilde{\boldsymbol{F}}]^t \cdot \widetilde{\boldsymbol{F}}$. For more details see [3].

2 WEAK FORMULATION

2.1 Principle of virtual power

In the second step, we define virtual power with respect to the deformation field $\boldsymbol{\varphi}$ as,

$$\delta_* \mathcal{P}_\varphi := \int_{t_n}^{t_{n+1}} \Big[\delta_* \dot{\mathcal{T}}_{kin}\left(\dot{\boldsymbol{\varphi}}, \dot{\boldsymbol{v}}, \dot{\boldsymbol{p}}\right) + \delta_* \dot{\Pi}_{ext}\left(\dot{\boldsymbol{\varphi}}, \boldsymbol{R}\right) + \delta_* \dot{\Pi}_{int}\left(\dot{\boldsymbol{\varphi}}, \dot{\widetilde{\boldsymbol{F}}}, \widetilde{\boldsymbol{P}}, \dot{\widetilde{\boldsymbol{C}}}, \widetilde{\boldsymbol{S}}, \dot{\widetilde{\boldsymbol{\Gamma}}}, \widetilde{\mathfrak{B}}, \dot{\widetilde{\boldsymbol{\Lambda}}}, \widetilde{\boldsymbol{A}}\right)\Big] \, dt = 0. \tag{2}$$

As in [4], the symbol δ_* is used in the sense of variation performed with respect to both temporally continuous time rate fields and temporally discontinuous Lagrange multiplier fields. The virtual inertial power with mass density ρ_0, velocity $\boldsymbol{v}$ and linear momentum $\boldsymbol{p}$ is defined by,

$$\delta_* \dot{\mathcal{T}} := \quad \int_{\boldsymbol{\mathcal{B}}_0} [\rho_0 \boldsymbol{v} - \boldsymbol{p}] \cdot \delta_* \dot{\boldsymbol{v}} \, dV - \int_{\boldsymbol{\mathcal{B}}_0} [\boldsymbol{v} - \dot{\boldsymbol{\varphi}}] \cdot \delta_* \dot{\boldsymbol{p}} \, dV + \int_{\boldsymbol{\mathcal{B}}_0} \dot{\boldsymbol{p}} \cdot \delta_* \dot{\boldsymbol{\varphi}} \, dV \tag{3}$$

Equation (4) shows the virtual internal power with new independent mixed field variables $\widetilde{\boldsymbol{F}}$ and $\widetilde{\boldsymbol{C}}$, energetically conjugated with independent first Piola-Kirchhoff stress tensor $\widetilde{\boldsymbol{P}}$ and second Piola-Kirchhoff stress tensor $\widetilde{\boldsymbol{S}}$, respectively. Similarly, $\widetilde{\boldsymbol{\Gamma}}$ and $\widetilde{\boldsymbol{\Lambda}}$ are energetically conjugated with independent $\widetilde{\mathfrak{B}}$ and $\widetilde{\boldsymbol{\Lambda}}$, respectively.

$$\begin{aligned}
\delta_* \dot{\Pi}_{int} := & \int_{\boldsymbol{B}_0} \left[\left(\widetilde{\mathfrak{B}} \odot_3 \frac{\partial(\nabla \dot{\widetilde{\boldsymbol{F}}})}{\partial \dot{\widetilde{\boldsymbol{F}}}}\right) + \left(\widetilde{\boldsymbol{A}} : \frac{\partial \boldsymbol{\Lambda}}{\partial \widetilde{\boldsymbol{F}}}\right) - \widetilde{\boldsymbol{P}}\right] : \delta_* \dot{\widetilde{\boldsymbol{F}}} \, dV - \int_{\boldsymbol{B}_0} \left[\dot{\widetilde{\boldsymbol{F}}} - \nabla \dot{\boldsymbol{\varphi}}\right] : \delta_* \widetilde{\boldsymbol{P}} \, dV \\
& + \int_{\boldsymbol{B}_0} \left[\widetilde{\boldsymbol{A}} : \frac{\partial \boldsymbol{\Lambda}}{\partial \widetilde{\boldsymbol{\Gamma}}} - \widetilde{\mathfrak{B}}\right] \odot_3 \delta_* \dot{\widetilde{\boldsymbol{\Gamma}}} \, dV - \int_{\boldsymbol{B}_0} \left[\dot{\widetilde{\boldsymbol{\Gamma}}} - \nabla \dot{\widetilde{\boldsymbol{F}}}\right] \odot_3 \delta_* \widetilde{\mathfrak{B}} \, dV + \int_{\boldsymbol{B}_0} \widetilde{\boldsymbol{P}} : \nabla[\delta_* \dot{\boldsymbol{\varphi}}] \, dV \\
& + \int_{\boldsymbol{B}_0} \left[\frac{\partial \Psi^{hg}(\widetilde{\boldsymbol{\Lambda}})}{\partial \widetilde{\boldsymbol{\Lambda}}} - \widetilde{\boldsymbol{A}}\right] : \delta_* \dot{\widetilde{\boldsymbol{\Lambda}}} \, dV - \int_{\boldsymbol{B}_0} \left[\dot{\widetilde{\boldsymbol{\Lambda}}} - \frac{\partial \boldsymbol{\Lambda}}{\partial \widetilde{\boldsymbol{F}}} : \dot{\widetilde{\boldsymbol{F}}} - \frac{\partial \boldsymbol{\Lambda}}{\partial \widetilde{\boldsymbol{\Gamma}}} \odot_3 \dot{\widetilde{\boldsymbol{\Gamma}}}\right] : \delta_* \widetilde{\boldsymbol{A}} \, dV \\
& - \int_{\boldsymbol{B}_0} \frac{1}{2} \left[\dot{\widetilde{\boldsymbol{C}}} - \dot{\widetilde{\boldsymbol{F}}^t} \widetilde{\boldsymbol{F}}\right] : \delta_* \widetilde{\boldsymbol{S}} \, dV + \int_{\boldsymbol{B}_0} \left[\frac{\partial \Psi^{ela}(\widetilde{\boldsymbol{C}})}{\partial \widetilde{\boldsymbol{C}}} - \frac{\widetilde{\boldsymbol{S}}}{2}\right] : \delta_* \widetilde{\boldsymbol{S}} \, dV
\end{aligned} \tag{4}$$

Here we represent triple contraction of tensors by $\odot_3$. The mass-specific body load $\boldsymbol{B}$ and a traction load $\bar{\boldsymbol{T}}$ on the Neumann boundary $\partial_T \boldsymbol{\mathcal{B}}_0$ are considered as external forces. Further, algorithmic stress tensors $\bar{\boldsymbol{S}}$ and $\bar{\boldsymbol{A}}$ are introduced in the external power functional to derive energy-momentum time integration. More details on this topic can be found in [5]. $\bar{\boldsymbol{\varphi}}$ denotes the prescribed boundary displacement with respect to the reaction force $\boldsymbol{R}$ as its associated Lagrange multiplier in the Dirichlet boundary $\partial_\varphi \boldsymbol{\mathcal{B}}_0$. These yield to the following virtual external power,

$$\begin{aligned}
\delta_* \dot{\Pi}_{ext} := & - \int_{\boldsymbol{\mathcal{B}}_0} \rho_0 \boldsymbol{B} \cdot \delta_* \dot{\boldsymbol{\varphi}} \, dV - \int_{\partial_T \boldsymbol{\mathcal{B}}_0} \bar{\boldsymbol{T}} \cdot \delta_* \dot{\boldsymbol{\varphi}} \, dA - \int_{\partial_\varphi \boldsymbol{\mathcal{B}}_0} \boldsymbol{R} \cdot \delta_* \dot{\boldsymbol{\varphi}} \, dA - \int_{\partial_\varphi \boldsymbol{\mathcal{B}}_0} [\dot{\boldsymbol{\varphi}} - \dot{\bar{\boldsymbol{\varphi}}}] \cdot \delta_* \boldsymbol{R} \, dA \\
& + \int_{\boldsymbol{\mathcal{B}}_0} \bar{\boldsymbol{A}} : \delta_* \dot{\widetilde{\boldsymbol{\Lambda}}} \, dV + \int_{\boldsymbol{\mathcal{B}}_0} \frac{1}{2} \bar{\boldsymbol{S}} : \delta_* \dot{\widetilde{\boldsymbol{C}}} \, dV
\end{aligned} \tag{5}$$

2.2 Weak forms

The resulting integrals of the weak forms of the extended Cauchy–Boltzmann continuum with fiber curvature is expressed in their continuous form in this paper for simplicity. The weak mechanical momentum equation is obtained as,

$$\int_{t_n}^{t_{n+1}}\int_{\boldsymbol{\mathcal{B}}_0} [\dot{\boldsymbol{p}} - \rho_0 \boldsymbol{B}] \cdot \delta_* \dot{\boldsymbol{\varphi}} \; dV dt - \int_{t_n}^{t_{n+1}}\int_{\partial_T \boldsymbol{\mathcal{B}}_0} \bar{\boldsymbol{T}} \cdot \delta_* \dot{\boldsymbol{\varphi}} \; dA dt \\ - \int_{t_n}^{t_{n+1}}\int_{\partial_\varphi \boldsymbol{\mathcal{B}}_0} \boldsymbol{R} \cdot \delta_* \dot{\boldsymbol{\varphi}} \; dA dt + \int_{t_n}^{t_{n+1}}\int_{\boldsymbol{\mathcal{B}}_0} \widetilde{\boldsymbol{P}} : \nabla[\delta_* \dot{\boldsymbol{\varphi}}] \; dV dt \; = \; 0. \tag{6}$$

To solve equation (6), the first Piola-Kirchhoff stress is required and determined from its weak form,

$$\int_{t_n}^{t_{n+1}}\int_{\boldsymbol{\mathcal{B}}_0} \left[\left(\widetilde{\mathfrak{B}} \odot_3 \frac{\partial(\nabla \dot{\widetilde{\boldsymbol{F}}})}{\partial \dot{\widetilde{\boldsymbol{F}}}} \right) + \left(\widetilde{\boldsymbol{A}} : \frac{\partial \boldsymbol{\Lambda}}{\partial \widetilde{\boldsymbol{F}}} \right) + \widetilde{\boldsymbol{F}} \widetilde{\boldsymbol{S}} - \widetilde{\boldsymbol{P}} \right] : \delta_* \dot{\widetilde{\boldsymbol{F}}} \; dV dt = \quad 0. \tag{7}$$

and stress tensors from their corresponding weak stress equations:

$$\int_{t_n}^{t_{n+1}}\int_{\boldsymbol{\mathcal{B}}_0} \left[2 \, \frac{\partial \Psi^{ela}}{\partial \widetilde{\boldsymbol{C}}} + \bar{\boldsymbol{S}} - \widetilde{\boldsymbol{S}} \right] : \delta_* \dot{\widetilde{\boldsymbol{C}}} dV dt = 0, \quad \int_{t_n}^{t_{n+1}}\int_{\boldsymbol{\mathcal{B}}_0} \left[\frac{\partial \Psi^{hg}}{\partial \widetilde{\boldsymbol{\Lambda}}} + \bar{\boldsymbol{A}} - \widetilde{\boldsymbol{A}} \right] : \delta_* \dot{\widetilde{\boldsymbol{\Lambda}}} dV dt = 0. \tag{8}$$

Linear momentum needed in the weak mechanical momentum equation (6) can be obtained by dissolving weak velocity equation into weak momentum equation,

$$\int_{t_n}^{t_{n+1}}\int_{\boldsymbol{\mathcal{B}}_0} [\boldsymbol{v} - \dot{\boldsymbol{\varphi}}] \cdot \delta_* \dot{\boldsymbol{p}} \; dV dt = 0, \qquad \int_{t_n}^{t_{n+1}}\int_{\boldsymbol{\mathcal{B}}_0} [\rho_0 \boldsymbol{v} - \boldsymbol{p}] \cdot \delta_* \dot{\boldsymbol{v}} \; dV dt = 0. \tag{9}$$

3 Space-time discretization

The weak forms are spatially and temporally discretized on the elemental level by Gaussian quadrature using Lagrangian ansatz funtions. The time rate variable fields $(\bullet)_i^{e,n}$ are approximated on the n-th time step by $k+1$-th order Lagrange polynomials corresponding to the normalized time $\alpha(t)$ on each time step $[t_n, t_{n+1}]$ such that,

$$(\bullet)^{h,n} = \sum_{i=1}^{k+1} M_i(\alpha) (\bullet)_i^{e,n}, \qquad \alpha(t) := \frac{t - t_n}{h_n} \in [0,1], \qquad h_n := t_{n+1} - t_n, \tag{10}$$

and the stress fields as well as Lagrange multiplier fields are $(\tilde{\bullet})_i^{e,n}$ are approximated on the n-th time step by k-th order Lagrange polynomials by

$$(\tilde{\bullet})^{h,n} = \sum_{i=1}^{k} \tilde{M}_i(\alpha) (\tilde{\bullet})_i^{e,n}, \qquad M_i(\alpha) = \prod_{\substack{j=1 \\ j \neq i}}^{k+1} \frac{\alpha - \alpha_j}{\alpha_i - \alpha_j}, \; 1 \leq i \leq k+1. \tag{11}$$

Similarly e-th finite element are approximated in space using standard local shape functions $N^A(\xi)$, $A = 1, \cdots, n_{node}$ defined on the reference domain. The resulting tangent matrix is condensated to pure displacement form by staggering the solution of globally discontinuous mixed fields on the elemental level. The implementation is performed in our In-house finite element code 'fEMcon' and the resulting linear systems of equations are solved using PARDISO solver.

3.1 Algorithmic stress tensor for fiber curvature strain

Analogous to [5], we introduce algorithmic stress tensors such that it corrects the error in the gradient theorem of the strain energy function. These stress tensors contribute to the total potential energy balance on each timestep $[t_n, t_{n+1}]$ by satisfying the gradient equation,

$$\mathcal{G}_{\widetilde{\boldsymbol{\Lambda}}}(\bar{\boldsymbol{A}}) := \Psi(\widetilde{\boldsymbol{\Lambda}}_{n+1}) - \Psi(\widetilde{\boldsymbol{\Lambda}}_n) - \int_{t_n}^{t_{n+1}} \left[\frac{\partial \Psi(\widetilde{\boldsymbol{\Lambda}})}{\partial \widetilde{\boldsymbol{\Lambda}}} + \bar{\boldsymbol{A}}\right] : \dot{\widetilde{\boldsymbol{\Lambda}}}\ dt = 0 \tag{12}$$

The stress tensor $\bar{\boldsymbol{A}}$ is determined by means of an isoperimetric variational problem associated with the Lagrange functional,

$$\mathcal{L}\left(\bar{\boldsymbol{A}}, \lambda_{\widetilde{\boldsymbol{\Lambda}}}\right) := \mathcal{F}_{\widetilde{\boldsymbol{\Lambda}}}\left(\bar{\boldsymbol{A}}\right) \ + \ \lambda_{\widetilde{\boldsymbol{\Lambda}}}\, \mathcal{G}_{\widetilde{\boldsymbol{\Lambda}}}\left(\bar{\boldsymbol{A}}\right), \qquad \text{where} \quad \mathcal{F}_{\widetilde{\boldsymbol{\Lambda}}}\left(\bar{\boldsymbol{A}}\right) := \frac{1}{2}\int_0^1 \bar{\boldsymbol{A}} : \bar{\boldsymbol{A}}\ d\alpha \tag{13}$$

$\lambda_{\widetilde{\boldsymbol{\Lambda}}}$ is the lagrange multiplier which enforces the constraint $\mathcal{G}_{\widetilde{\boldsymbol{\Lambda}}}$ with respect to the minimization function $\mathcal{F}_{\widetilde{\boldsymbol{\Lambda}}}\left(\bar{\boldsymbol{A}}\right)$. The algorithmic stress tensors $\bar{\boldsymbol{A}}$ then yields the form,

$$\bar{\boldsymbol{A}} := \frac{\Psi(\widetilde{\boldsymbol{\Lambda}}_{n+1}) - \Psi(\widetilde{\boldsymbol{\Lambda}}_n) - \int_0^1 \frac{\partial \Psi(\widetilde{\boldsymbol{\Lambda}})}{\partial \widetilde{\boldsymbol{\Lambda}}} : \dot{\widetilde{\boldsymbol{\Lambda}}}}{\int_0^1 \dot{\widetilde{\boldsymbol{\Lambda}}} : \dot{\widetilde{\boldsymbol{\Lambda}}}}\ \dot{\widetilde{\boldsymbol{\Lambda}}}, \tag{14}$$

In the similar way $\bar{\boldsymbol{S}}$ is dervied with respect to $\widetilde{\boldsymbol{C}}$ and is given by

$$\bar{\boldsymbol{S}} := \frac{\Psi(\widetilde{\boldsymbol{C}}_{n+1}) - \Psi(\widetilde{\boldsymbol{C}}_n) - \int_0^1 \frac{\partial \Psi(\widetilde{\boldsymbol{C}})}{\partial \widetilde{\boldsymbol{C}}} : \dot{\widetilde{\boldsymbol{C}}}}{\int_0^1 \dot{\widetilde{\boldsymbol{C}}} : \dot{\widetilde{\boldsymbol{C}}}}\quad \dot{\widetilde{\boldsymbol{C}}}. \tag{15}$$

4 BALANCE LAWS

With the introduction of new independent field variables, the extended standard Cauchy continuum has to fulfill physical balance laws. The total momentum and energy is conserved at every discrete time step with a special numerical treatment by considering real functions as test functions in place of virtual functions. Following the steps in [5], by performing virtual translations along a constant vector $\boldsymbol{c}$, choosing the test function $\delta_*\dot{\boldsymbol{\varphi}} = \boldsymbol{c}$, the balance of total linear momentum is obtained as

$$\boldsymbol{\mathcal{L}}_{n+1} \ - \ \boldsymbol{\mathcal{L}}_n \ = \ \int_{t_n}^{t_{n+1}}\!\!\int_{\boldsymbol{\mathcal{B}}_0} \rho_0 \boldsymbol{B}\ dV dt + \int_{t_n}^{t_{n+1}}\!\!\int_{\partial_T \boldsymbol{\mathcal{B}}_0} \bar{\boldsymbol{T}}\ dA\ dt + \int_{t_n}^{t_{n+1}}\!\!\int_{\partial_\varphi \boldsymbol{\mathcal{B}}_0} \boldsymbol{R}\ dA\ dt \tag{16}$$

Similarly, choosing test function $\delta_*\dot{\boldsymbol{\varphi}} = \boldsymbol{c} \times \boldsymbol{\varphi}$ in (6) for an arbitrary constant axial vector $\boldsymbol{c}$ and eliminating the first Piola-Kirchhoff tensor yields a time integrator that eventually conserves total angular momentum,

$$\begin{aligned}\boldsymbol{\mathcal{J}}_{n+1} - \boldsymbol{\mathcal{J}}_n = &\int_{t_n}^{t_{n+1}}\!\!\int_{\boldsymbol{\mathcal{B}}_0} \left[\boldsymbol{\varphi} \times \rho_0 \boldsymbol{B}\right]\ dV dt + \int_{t_n}^{t_{n+1}}\!\!\int_{\partial_T \boldsymbol{\mathcal{B}}_0} \left[\boldsymbol{\varphi} \times \bar{\boldsymbol{T}}\right] dA dt + \int_{t_n}^{t_{n+1}}\!\!\int_{\partial_\varphi \boldsymbol{\mathcal{B}}_0} \left[\boldsymbol{\varphi} \times \boldsymbol{R}\right] dA dt \\ &+ \int_{t_n}^{t_{n+1}}\!\!\int_{\boldsymbol{\mathcal{B}}_0} \boldsymbol{\epsilon} : \left[\left(\widetilde{\mathfrak{B}} \odot_3 \frac{\partial(\nabla \dot{\widetilde{\boldsymbol{F}}})}{\partial \dot{\widetilde{\boldsymbol{F}}}}\right) + \left(\widetilde{\boldsymbol{A}} : \frac{\partial \boldsymbol{\Lambda}}{\partial \widetilde{\boldsymbol{F}}}\right) + \widetilde{\boldsymbol{F}}\widetilde{\boldsymbol{S}}\right] \widetilde{\boldsymbol{F}}^t\ dV dt\end{aligned} \tag{17}$$

The balance law corresponding to the potential energy associated with body load $\boldsymbol{B}$

$$\mathcal{P} := \int_{\boldsymbol{\mathcal{B}}_0} \left[\Psi^{total}\right] dV - \int_{\boldsymbol{\mathcal{B}}_0} \boldsymbol{\varphi} \cdot \rho_0 \boldsymbol{B} dV \tag{18}$$

is obtained by means of the algorithmic stress tensors in (14) and (15) along with the choice of test functions $\delta_* \dot{\widetilde{\boldsymbol{C}}} = \dot{\widetilde{\boldsymbol{C}}}$, $\delta_* \dot{\widetilde{\boldsymbol{\Lambda}}} = \dot{\widetilde{\boldsymbol{\Lambda}}}$ and $\delta_* \widetilde{\boldsymbol{S}} = \widetilde{\boldsymbol{S}}$, $\delta_* \widetilde{\boldsymbol{A}} = \widetilde{\boldsymbol{A}}$, respectively.

$$\mathcal{P}_{n+1} \; - \; \mathcal{P}_n \; = \; \int_{t_n}^{t_{n+1}} \int_{\boldsymbol{\mathcal{B}}_0} \left[\widetilde{\boldsymbol{A}} : \dot{\widetilde{\boldsymbol{\Lambda}}} + \frac{1}{2} \, \widetilde{\boldsymbol{S}} : \left(\widetilde{\boldsymbol{F}}^t \dot{\widetilde{\boldsymbol{F}}} + \dot{\widetilde{\boldsymbol{F}}}^t \widetilde{\boldsymbol{F}} \right) \right] dV dt - \int_{t_n}^{t_{n+1}} \int_{\boldsymbol{\mathcal{B}}_0} \dot{\boldsymbol{\varphi}} \cdot \rho_0 \boldsymbol{B} dV dt \tag{19}$$

Furthermore, employing different choice of suitable test function for $\delta_* \dot{\boldsymbol{\varphi}} = \dot{\boldsymbol{\varphi}}$ and eliminating the first Piola-Kirchhoff tensor, we derive the total kinetic energy conserving time integrator as,

$$\begin{aligned} \boldsymbol{\mathcal{K}}_{n+1} \; - \; \boldsymbol{\mathcal{K}}_n \; = \; & \int_{t_n}^{t_{n+1}} \int_{\boldsymbol{\mathcal{B}}_0} \dot{\boldsymbol{\varphi}} \cdot \rho_0 \boldsymbol{B} \; dV dt \; + \; \int_{t_n}^{t_{n+1}} \int_{\partial_T \boldsymbol{\mathcal{B}}_0} \dot{\boldsymbol{\varphi}} \cdot \bar{\boldsymbol{T}} \; dA \; dt \; + \; \int_{t_n}^{t_{n+1}} \int_{\partial_\varphi \boldsymbol{\mathcal{B}}_0} \dot{\boldsymbol{\varphi}} \cdot \boldsymbol{R} \; dA \; dt \\ & - \int_{t_n}^{t_{n+1}} \int_{\boldsymbol{\mathcal{B}}_0} \left[\left(\widetilde{\mathfrak{B}} \odot_3 \frac{\partial (\nabla \dot{\widetilde{\boldsymbol{F}}})}{\partial \dot{\widetilde{\boldsymbol{F}}}} \right) + \left(\widetilde{\boldsymbol{A}} : \frac{\partial \boldsymbol{\Lambda}}{\partial \widetilde{\boldsymbol{F}}} \right) + \widetilde{\boldsymbol{F}} \widetilde{\boldsymbol{S}} \right] : \dot{\widetilde{\boldsymbol{F}}}^t \; dV dt \end{aligned} \tag{20}$$

And then we arrive at total energy balance as, $\dot{\boldsymbol{\mathcal{H}}} := \dot{\boldsymbol{\mathcal{K}}} + \dot{\mathcal{P}}$

$$\boldsymbol{\mathcal{H}}_{n+1} \; - \; \boldsymbol{\mathcal{H}}_n \quad = \quad \int_{t_n}^{t_{n+1}} \int_{\partial_T \boldsymbol{\mathcal{B}}_0} \dot{\boldsymbol{\varphi}} \cdot \bar{\boldsymbol{T}} \; dA \; dt \; + \; \int_{t_n}^{t_{n+1}} \int_{\partial_\varphi \boldsymbol{\mathcal{B}}_0} \dot{\boldsymbol{\varphi}} \cdot \boldsymbol{R} \; dA \; dt \tag{21}$$

5 NUMERICAL EXAMPLES

In our numerical investigation, we apply our newly developed continuum formulation with strains associated to fiber curvature to representative numerical examples and study the balance laws and evolution of time dependent properties for the chosen mechanical system.

5.1 Oscillation of Cooks beam

A fiber reinforced Cook's cantilever beam is spatially discretized by 20-noded tri-quadratic serendipity elements and is simply supported on its left end such that the displacement of nodes at this boundary are fixed in all three directions $\boldsymbol{e}_1, \boldsymbol{e}_2, \boldsymbol{e}_3$. The beam is self-excited by its body weight due to the gravitational load. Table 1 provides the data used in the simulation. For temporal discretization a Lagrange polynomial of order $k = 2$ is used as explained in section 2.2 and the strain energy function as described in (1). It is to be noted that the reaction forces $\boldsymbol{R}$ at the dirichlet boundary nodes are taken into account. We compare the results obtained from simulations with and without the influence of the algorithmic stress tensors for the fiber curvature strain and the tension strain in Figure 4. It can been observed that the total linear momentum is well conserved by virtue of its definition and our new time integrator for angular momentum in (17) consistently conserves the total angular momentum. In the case of total energy consistence, the modified time integrator in (19) and (20) together brings in the conservation of total energy (21) for the variant with algorithmic stress tensors (14) and (15). On the other hand, the simulation variant without the same makes time integrators incapable of conserving energy for the chosen time step size and the Newton Raphson tolerance Tol .

5.2 Free flying L-block

Our second example is inspired from the work [7]. A fiber reinforced L-shaped block is spatially discretized with 117 tri-linear finite elements. As an initial condition, two equal and opposite traction forces are applied on the boundary surfaces as shown in Figure 5. The traction forces are given as a hat function of time $f(t)$ and the corresponding traction vectors are given by

$$\bar{\boldsymbol{t}}_a = -\bar{\boldsymbol{t}}_b = f(t) \begin{bmatrix} 256/9 \\ 512/9 \\ 768/9 \end{bmatrix} \text{Pa}, \qquad f(t) = \begin{cases} t & \text{for } 0\text{s} \leq t \leq 2\text{s} \\ 4-t & \text{for } 2\text{s} \leq t \leq 4\text{s} \\ 0 & \text{for } t \geq 4\text{s}. \end{cases}$$

No external torque is acting on the block after the loading phase and the block tumbles constantly as there is no gravitational force or any other external loads after the loading phase. Quadratic of the curvature I_6^2 is chosen with an aim to use an non-linear energy function of Ψ^{hg} in the simulation. Due to the equal and opposite traction forces in the loading phase, the linear momentum is equilibriated and hence the total linear momentum is a conserved quantity, which can be observed in the momentum maps in Figure 6. With respect to the angular momentum, the corresponding improved time integrator (17) takes into account the internal couples arising due to the fiber curvature and conserves the total angular momentum. Consequently with the enhanced conjugate gradient in higher-order time approximation the new energy time integrators are capable to exactly conserve total energy consistently up to the chosen Newton Raphson tolerance Tol for both temporal approximations $k = 1$ and $k = 2$.

5.3 Noel's turbine rotor

In this example we simulate a slender fiber reinforced turbine rotor that undergoes large rotations and here we would like to show that our new time integrators preserve the time evolutions of the energies and momenta. For the sake of brevity, we refer to [1] for the construction of the rotor and fiber orientation definitions and load setup are analogous to [4]. In contrast to these references, no stator is considered and only a mechanical system without initial velocity is considered here. The simulation has been performed using 5488 tri-linear hexahedral elements with a temporal approximation $k = 2$ along with algorithmic stress tensors. The front side of blades are loaded with a hydrodynamic pressure $f_p(t) = \hat{p}|\sin(\omega\ t)|$ as follower loads without any dirichlet boundary conditions. The simulation is performed according to the parametrs provided in Table 3. As expected the rotor translates in the negative z-direction with constantly increasing velocity by the virtue of evolution of follower forces with respect to the flat blades due to the pressure load. This can be evidently seen in the linear momentum plot in Figure 9. In the same way, increasing angular momentum about z-direction is expected as there is no opposing dirichlet boundary and the same is reflected in the angular momentum plot. Similar trend is observed in the energy plots where the kinetic and potential energy are increasing due to the accelration of the rotor.

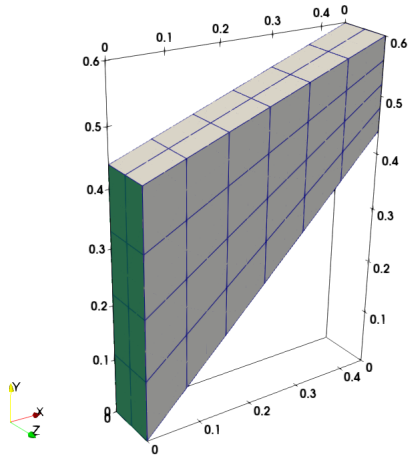

Figure 2: Simply supported beam subjected to gravitational load.

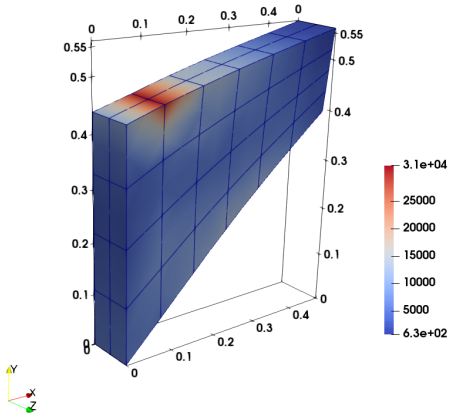

Figure 3: Current configuration of the beam at T = 2.15s with Von-Mises stress.

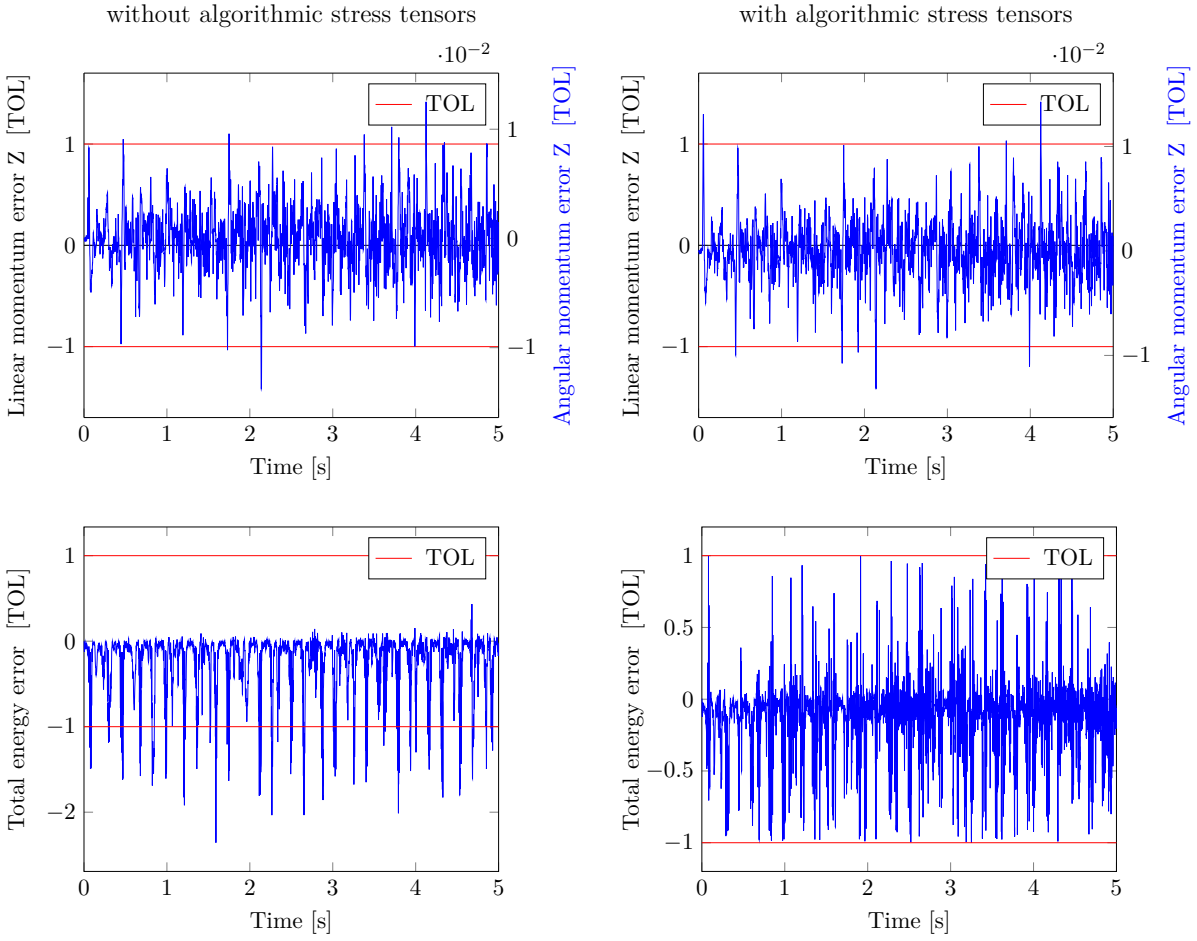

Figure 4: Comparison of energy and momentum consistence without(left) and with algorithmic stress tensors(right) of fiber-reinforced cantilver beam with $n_{el} = 48$ quadratic hexahedral elements for time polynomial of order $k = 2$ and a Newton-Raphson tolerance TOL.

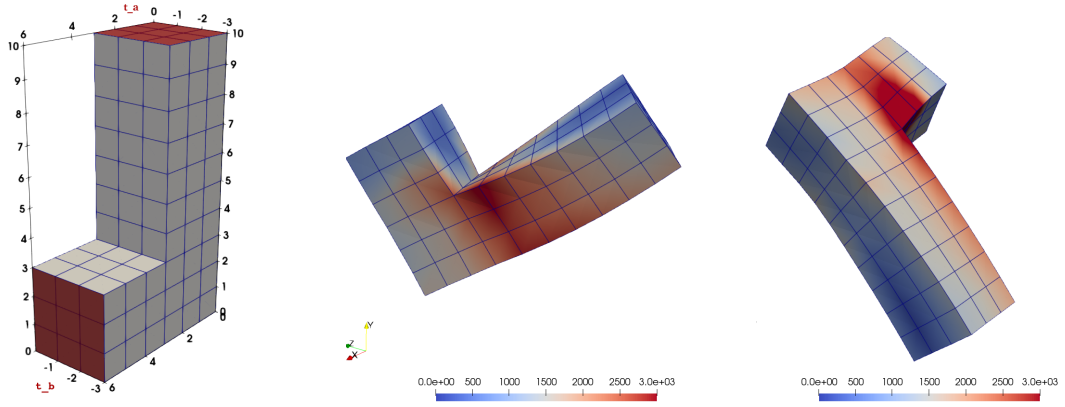

Figure 5: Free-flying L-block subjected to traction load $\bar{\boldsymbol{t}}_a$ and $\bar{\boldsymbol{t}}_b$ on red surfaces at time $T = 0$s(Left), current configurations at time $T = 12.5$s(middle) and at time $T = 25$s(right) indicating Von-Mises stress.

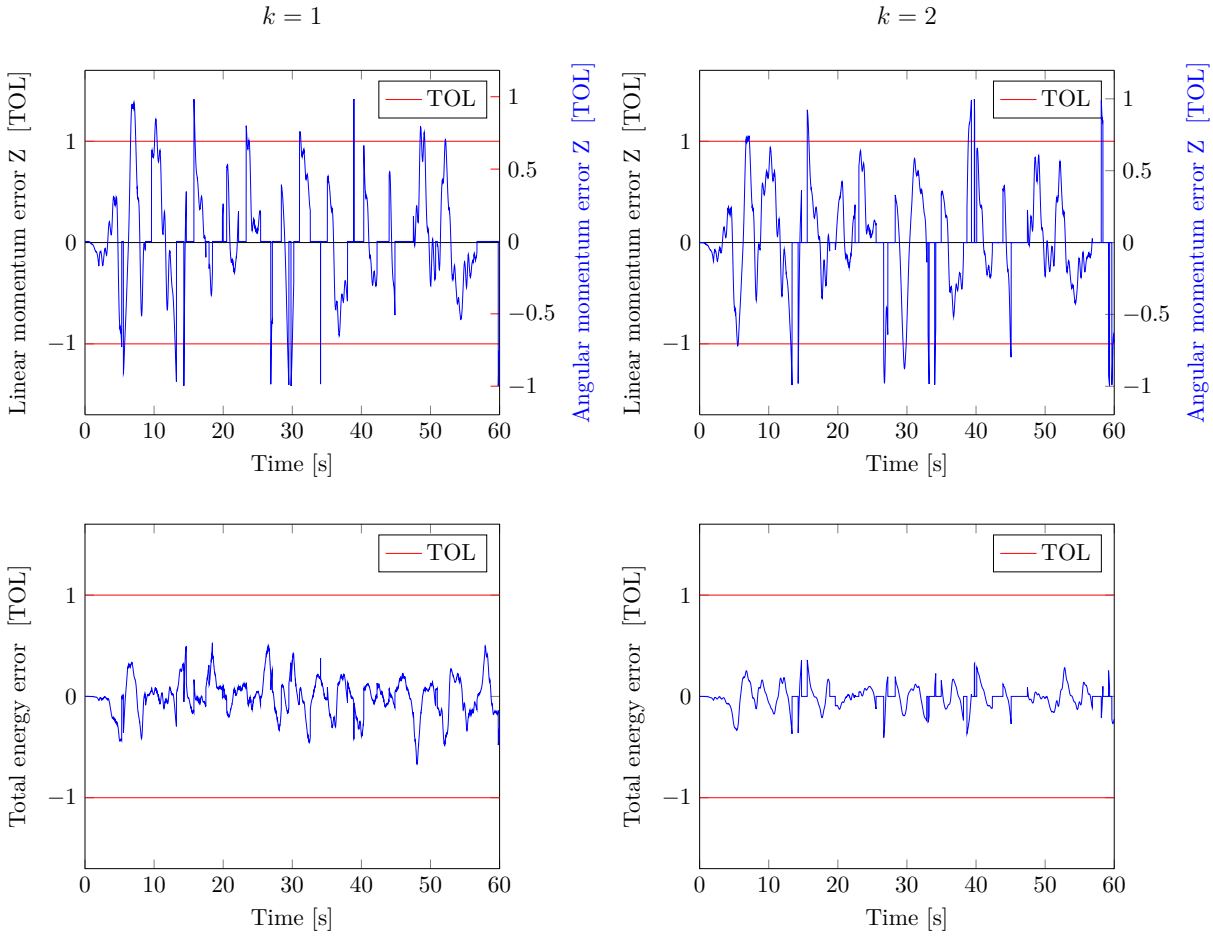

Figure 6: Comparison of energy consistence with algorithmic stress tensors of fiber-reinforced L-shaped block with $n_{el} = 117$ linear hexahedral elements for time polynomials of order $k = 1$ and $k = 2$.

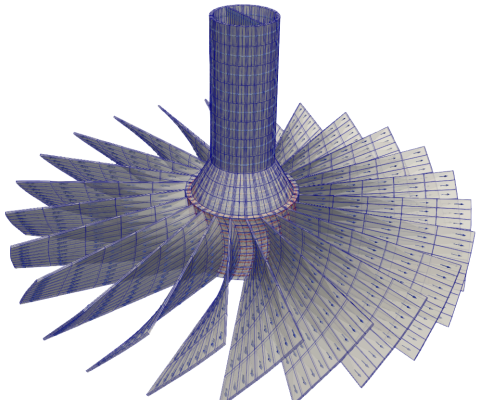

Figure 7: Fiber reinforced turbine rotor subjected to hydrostatic pressure load on blades.

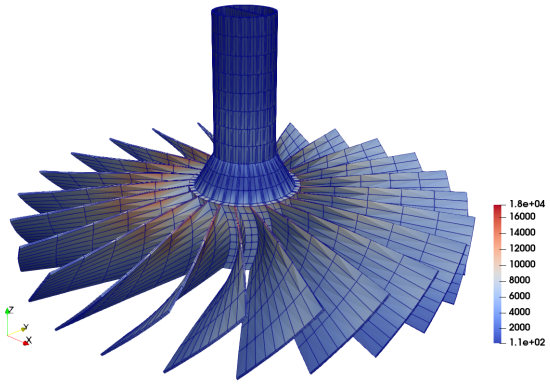

Figure 8: Current configuration of turbine at T=5s indicating Von-Mises stress.

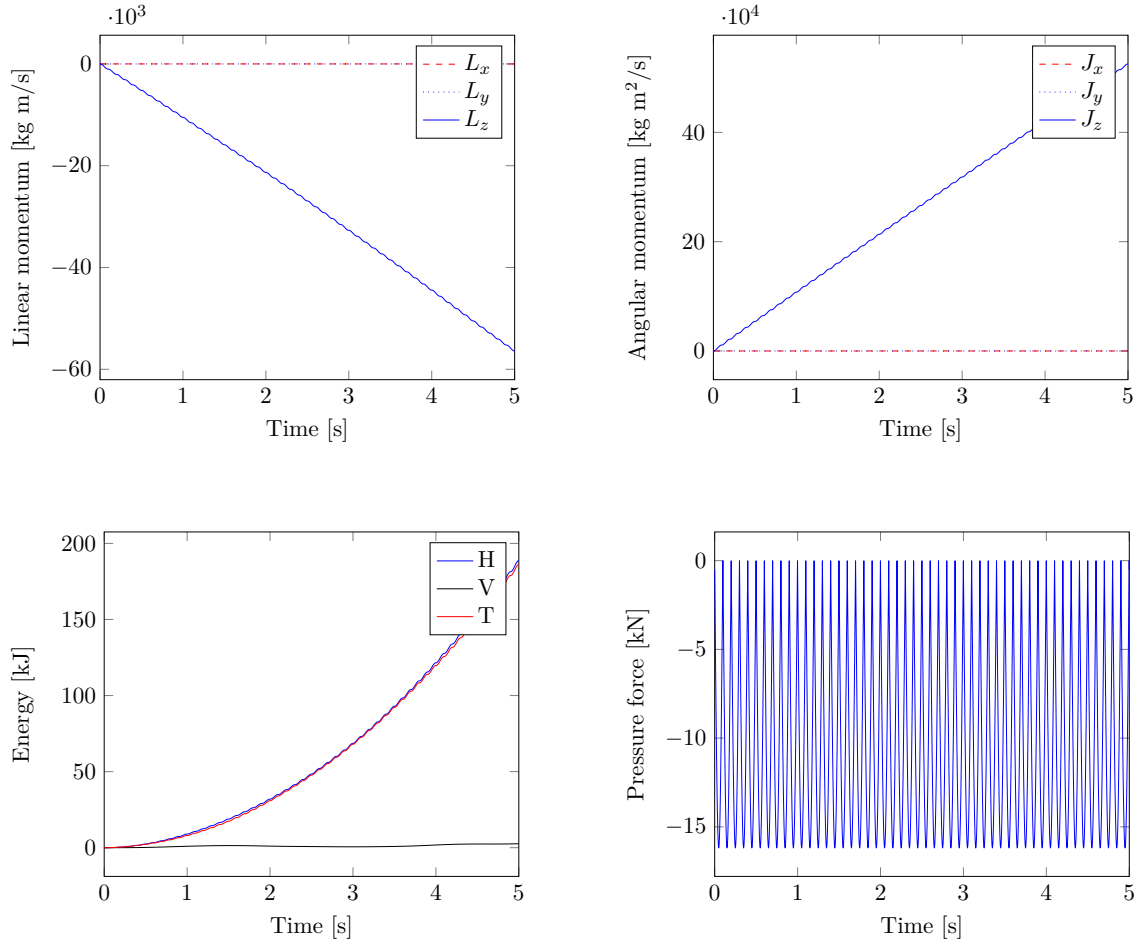

Figure 9: Time evolution of momenta, energies and external load for Fiber-reinforced turbine rotor with $n_{el} = 5488$ linear hexahedral elements and temporal approximation of order $k = 2$.

6 SUMMARY

In this work we derive an extended continuum using a mixed finite element formulation by introducing an independent field variable for fibre curvature strain in the continuum to capture the fiber curvature effect. This leads to the introduction of a local bending stiffness by an additional strain energy function based on fiber curvature. We then derive new time integrators for the total energy and total momentum consistence and implement it with higher order time approximation. By deriving an energy-momentum scheme from the principle of virtual power for the proposed mixed element formulation, we have devised a method that significantly reduce the modelling errors arising due to unaccounted fiber stiffness in numerical simulations. And this helps in improving the strength-to-weight ratio of fiber reinforced composites in the design process. From the evidence of the demonstrated numerical examples, we claim that our new time integrators provides us physically consisitent dynamic behaviour which can be observed from the preservation of balance laws and the time evolution of energies and momenta. To further our research we intend to extend our formulation to solve dynamic thermo-mechanical problems.

Acknowledgments This research was made possible by the DFG under grants GR 3297/6-1 and GR 3297/4-2, which is gratefully acknowledged.

REFERENCES

[1] Noels, L., Stainier, L. and Ponthot, J.-P., A Consistent Dissipative Time Integration Scheme for Structural Dynamics: Application to Rotordynamics. *45th AIAA/ASME/ASCE/AHS/ASC Structures, Structural Dynamics & Materials Conference*, pp. 1945, (2004).

[2] Madeo, A., Ferretti, M., dell'Isola, F. and Boisse, P. A Thick fibrous composite reinforcements behave as special second-gradient materials: three-point bending of 3D interlocks. *Z. Angew. Math. Phys.*, Vol. **66**, pp. 2041–2060, (2015).

[3] Asmanoglo, T. and Menzel, A. A multi-field finite element approach for the modelling of fibre-reinforced composites with fibre-bending stiffness. *Comput. Methods Appl.Mech. Engrg.*, Vol. **317**, pp. 1037–1067, (2017).

[4] Groß, M. and Dietzsch, J. Variational-based locking-free energy–momentum schemes of higher-order for thermo-viscoelastic fiber-reinforced continua. *Comput. Methods Appl.Mech. Engrg.*, Vol. **343**, pp. 631–671, (2019).

[5] Groß, M., Dietzsch, J. and Röbiger, C., Non-isothermal energy–momentum time integrations with drilling degrees of freedom of composites with viscoelastic fiber bundles and curvature–twist stiffness. *Comput. Methods Appl.Mech. Engrg.*, Vol. **365**, 112973, (2020).

[6] Kalaimani, I., Dietzsch, J. and Gross, M. Modeling of fiber-bending stiffness in fiber-reinforced composites with a dynamic mixed finite element method based on the principle of virtual power. *Proc. Appl. Math. Mech.*, Vol. **21**, pp. e202100006 , (2021).

[7] Schiebl, M., and Betsch, P., Structure-preserving space-time discretization of large-strain thermo-viscoelasticity in the framework of GENERIC. *Int J Numer Methods Eng.*, Vol. **122**, pp. 3448–3488, (2021).

A Simulation data

The chosen material and simulation parameters are in SI units.

Table 1: Simulation data for Cooks beam

Material Parameters	
μ	$0.1 \cdot 10^6$
λ	$100 \cdot 10^6$
l^2	$5 \cdot 10^{-5}$
ρ_0	10^3
Neumann load	-
Dirichlet load	(x,y,z)-dof fixed
Fiber orientation $\boldsymbol{a}_0$	$\boldsymbol{e}_x$
Initial velocity $\boldsymbol{v}_0$	0
Newton tolerance Tol	10^{-5}
Time step size h_n	0.001
Simulation duration T	5
Standard gravity	$g = 9.81$ with $\boldsymbol{e}_g = -\boldsymbol{e}_y$

Table 2: Simulation data for L-block

Material Parameters	
μ	$0.1 \cdot 10^5$
λ	$100 \cdot 10^5$
l^2	$1 \cdot 10^{-2}$
ρ_0	10^3
Neumann load	$t_a = -t_b$
Dirichlet load	-
Fiber orientation $\boldsymbol{a}_0$	$\boldsymbol{e}_x$
Initial velocity $\boldsymbol{v}_0$	0
Newton tolerance Tol	10^{-4}
Time step size h_n	0.01
Simulation duration T	60
Standard gravity	$g = 0$ with $\boldsymbol{e}_g = -\boldsymbol{e}_y$

Table 3: Simulation data for turbine rotor

Material Parameters		Fiber orientations	
μ	$0.1 \cdot 10^6$	$\boldsymbol{a}_0^{bla}$	along the blade profile
λ	$100 \cdot 10^6$	$\boldsymbol{a}_0^{sha}$	$\boldsymbol{e}_z \times \frac{r}{\|\|r\|\|}$
l^2	$1 \cdot 10^{-4}$	$\boldsymbol{a}_0^{bak}$	$\boldsymbol{e}_y$
ρ_0	10^3	$\boldsymbol{a}_0^{frt}$	$\boldsymbol{e}_x$
Neumann load $f_p(t)$	$\hat{p}\|\sin(\omega\ t)\|$	Newton tolerance Tol	10^{-2}
$\hat{p}$	100	Time step size h_n	0.001
ω	10π	Standard gravity	$g = 0$ with $\boldsymbol{e}_g = -\boldsymbol{e}_z$
Dirichlet load	-	Initial velocity $\boldsymbol{v}_0$	0
Simulation duration T	5		